

A comprehensive chemical model for the preliminary steps of thermal stabilization process in carbon fibre manufacturing line

Khashayar Badii^{a,1}, Gelayol Golkarnarenji^a, Abbas S. Milani^b, Minoos Naebe^c, Hamid Khayyam^d

^a School of Engineering, Deakin University, Waurn Ponds, VIC 3216, Australia

^b Composites Research Network, School of Engineering, University of British Columbia, Canada

^c Institute for Frontier Materials, Carbon Nexus, Deakin University, Waurn Ponds, VIC 3216, Australia

^d School of Engineering, RMIT University, Melbourne, VIC 3000, Australia

A1. Thermal stabilisation process:

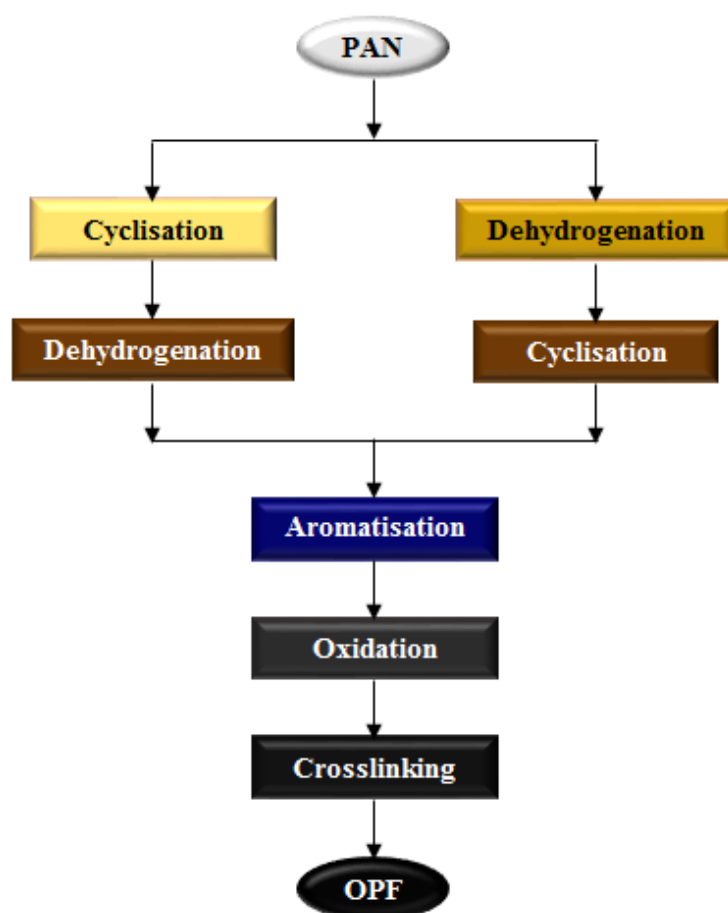


Fig. A1. A five-reaction-set series-parallel mechanism [1-4].

¹ Corresponding Author: khashayar.badii@deakin.edu.au (Khashayar Badii)

A2. Structure of oxidized PAN fibre (OPF):

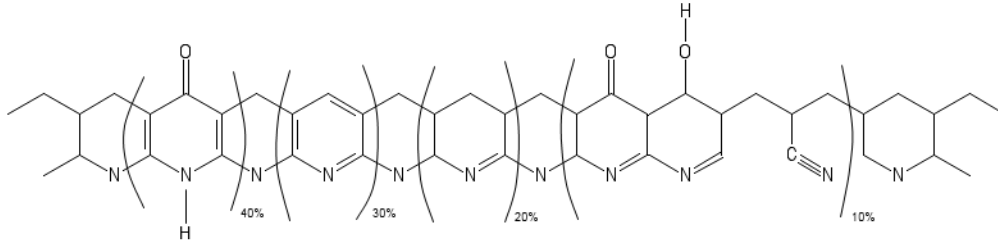


Fig. A2. A demo for the final product (OPF) of the thermal oxidative stabilization process [3, 5-7].

A3. Kissinger and Flynn-Wall-Ozawa approaches:

For chemical reactions, Kissinger showed [8, 9]:

$$-\frac{E_a}{R} = \frac{d\left[\ln\left(\frac{\phi}{T_p^2}\right)\right]}{d\left(\frac{1}{T_p}\right)} \quad (\text{A1})$$

$$k_0 = \frac{\phi E_a}{RT_p^2} e^{\frac{E_a}{RT_p}} \quad (\text{A2})$$

where ϕ , E_a , k_0 , R , and T_p are the ramp or heating rate (K/min), activation energy ($J/kmol$), frequency factor ($(m^3)^{n-1}/s \cdot (kmol)^{n-1}$), Gas constant ($8,314 J/kmol/K$) and the absolute temperature at endothermic / exothermic peak (K), respectively. For Flynn-Wall-Ozawa (FWO) approach [10-12], k_0 is calculated by Equation A2, but the Equation A1 was revised as below:

$$-\frac{E_a}{R} = 2.19 \frac{d[\log(\phi)]}{d\left(\frac{1}{T_p}\right)} \quad (\text{A3})$$

A4. Suggested mechanism in Dunham-Edie chemical model

(DECM):

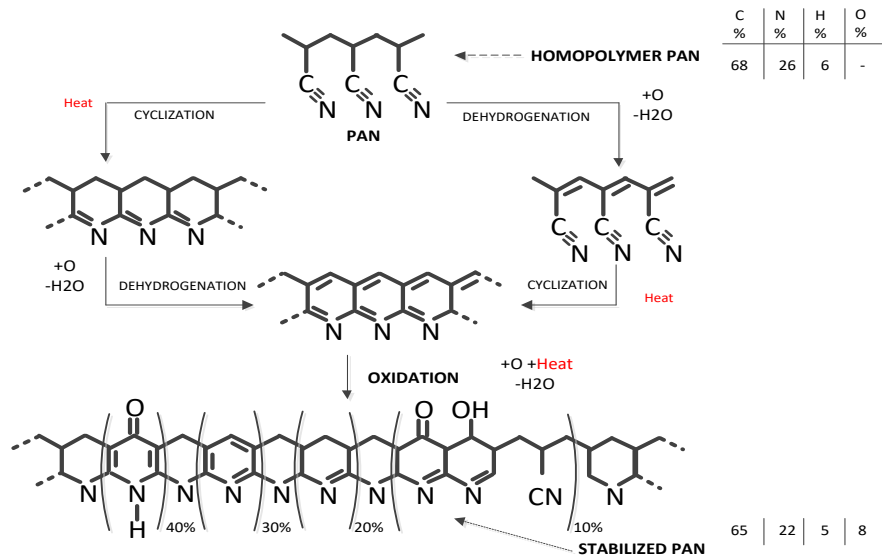


Fig. A3. Steps of DECM for degrading PAN precursor to cross-linked OPF, including cyclisation, dehydrogenation and oxidation sets of reactions [6, 13].

A5. Structure of monomers of PAN precursor (Blue Star):

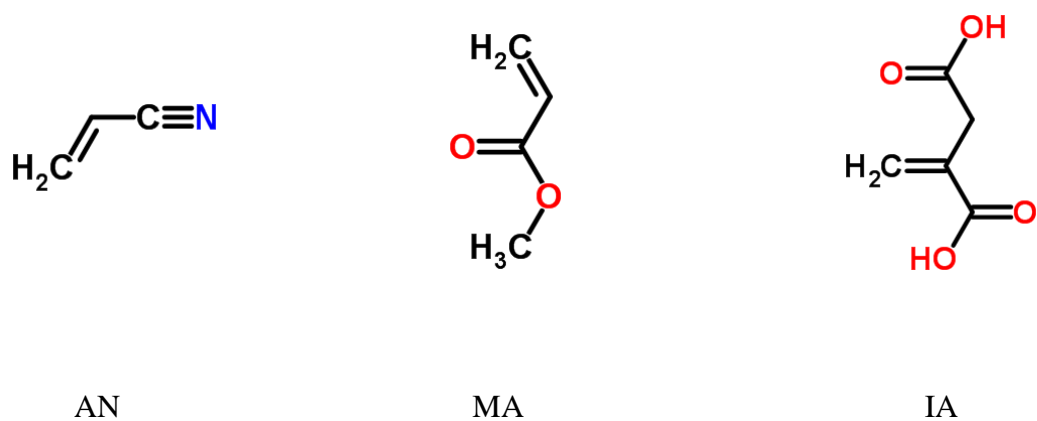


Fig. A4. Structures of acrylonitrile (AN), methyl acrylate (MA) and itaconic acid (IA) monomers [13].

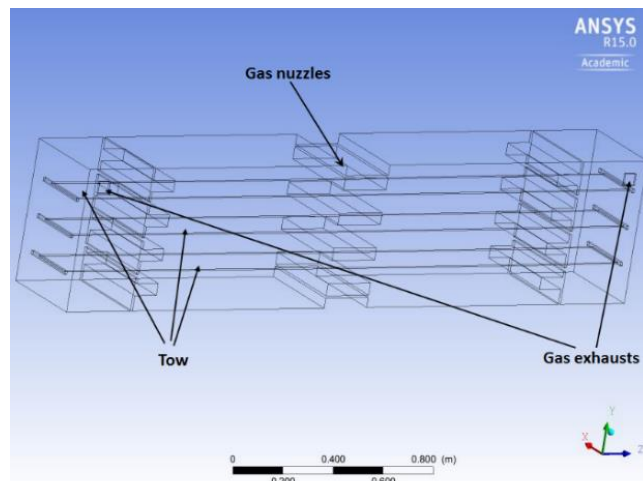
A6. Air flow and temperature distribution inside the reactor:

To investigate the uniformity of temperature inside reactor, the heat and momentum transfer equations [14] have been considered and solved based on the second order κ - ϵ model turbulence model and the structure of reactor by the ANSYS (R15.0) software.

The dimensions of the model have been presented in Table A1 (bigger than effective dimensions in Table 2). Fig. A5 shows the internal structure of the reactor. This is the back view of stabilisation reactor. The location of gas nuzzle and gas exhaust have been mentioned in this figure. There are two chambers in left and right to prevent gas leakage to outside by applying positive pressure. Gas can only leave the reactor at the exhaust point regarding the presence of toxic gases, such as HCN. The positions of temperature sensors and generated grid have been presented in Fig. A6.

Table A1. Dimensions of the first reactor of the single tow stabilisation process.

Dimension	Size, m
Length	2.6
Width	0.4
Height	0.6



Fig, A5. Structure of the model domain (internal structure of the reactor).

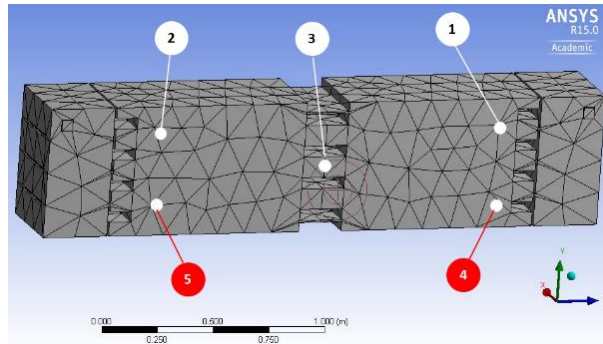


Fig. A6. Generated grid based on finite element method with the position of temperature sensors (1 to 5).

The model has been performed for four various scenarios based on temperature levels, 227°C, 230°C, 233°C, and 236°C. Fig. A7 and Fig. A8 present flow streamlines and gauge pressure distribution in the first scenario (inlet temperature at 227°C), respectively. The streamlines are almost uniform, particularly near the axis of the reactor (in the range of fibre tow). It means that the flow is turbulence, and the heat and mass transfer coefficients are sufficient big; therefore, the temperature and oxygen concentration near tow can be considered equal to the bulk of gas.

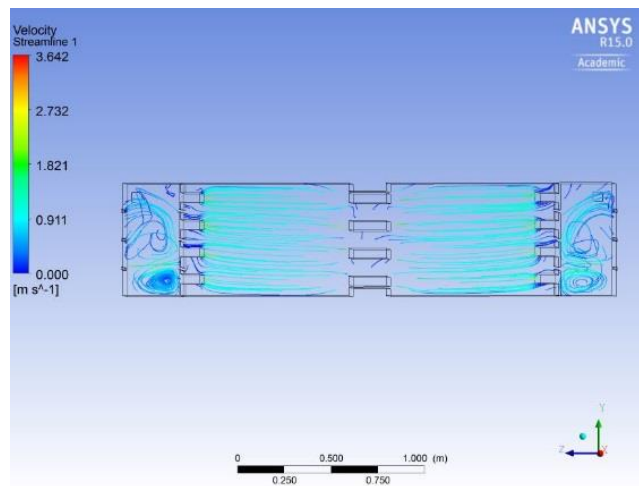


Fig. A7. Flow streamlines inside the reactor in the first case study (inlet temperature at 227°C).

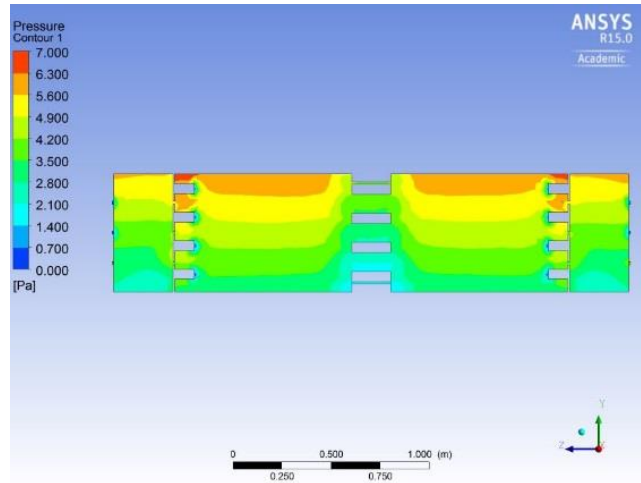


Fig. A8. Gauge pressure (Pa) distribution inside the reactor in the first case study (inlet temperature at 227°C).

Fig. A9 to Fig. A12 present the temperature distribution for four considered scenarios. The results of the modelling show that the temperature is uniform; hence, the momentum equation can be ignored. It is a significant assumption. This assumption can decrease the complexity of the model solution, the area of study, required memory, and calculation time dramatically.

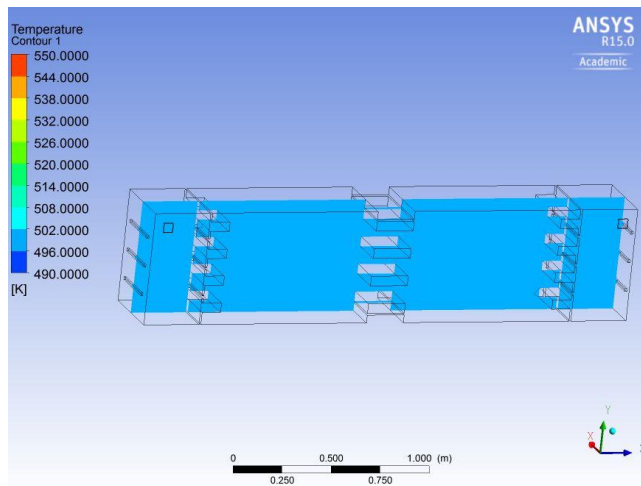


Fig. A9. Temperature distribution in the central plane at 227 °C (500.16 K) in the inlet.

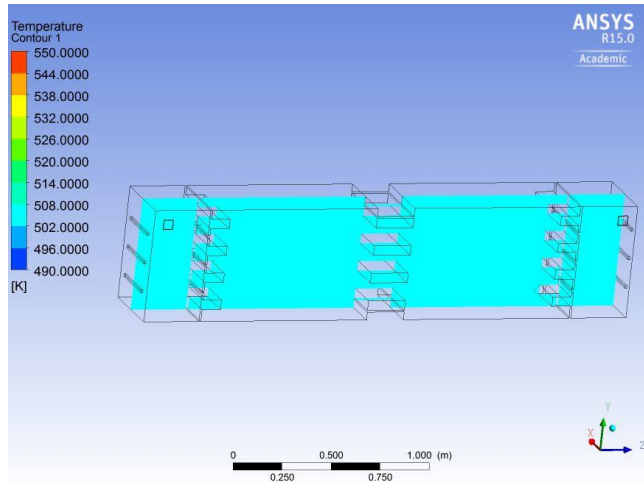


Fig. 10. Temperature distribution in the central plane at 230 °C (503.16 K) in the inlet.

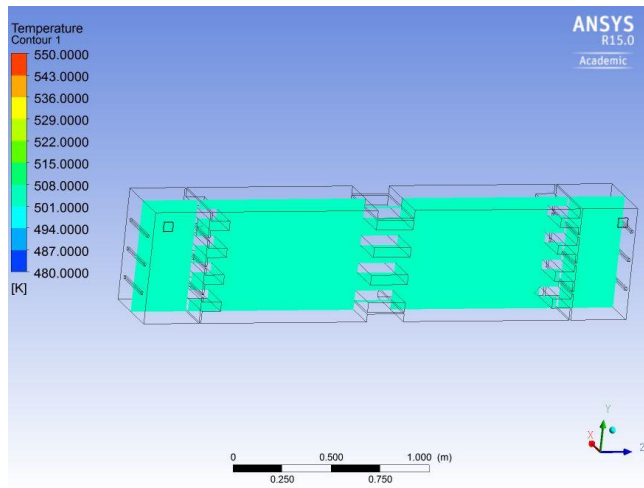


Fig. A11. Temperature distribution in the central plane at 233 °C (506.16 K) in the inlet.

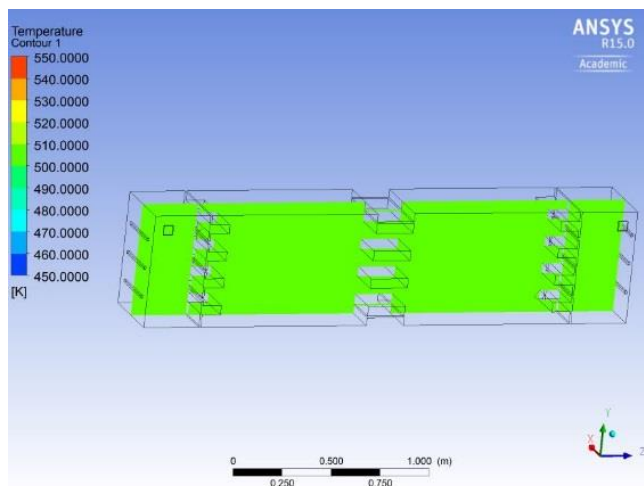


Fig. A12. Temperature distribution in the central plane at 236 °C (509.16 K) in the inlet.

The validation of the model was confirmed by experimental results. Stabilisation reactor has 5 temperature sensor. The position of these sensors has been shown in Fig. A6. The outcomes of validation have been presented in Table A2. The results show that there is a good agreement between model and experiments. The error of the model is less than 1.4%.

Table A2. Validation of the model in four different scenarios.

Temperature sensor no.	Case 1 (227°C)		Error, %	Case 2 (230°C)		Error, %	Case 3 (233°C)		Error, %	Case 4 (236°C)		Error, %
	Test	ANSYS		Test	ANSYS		Test	ANSYS		Test	ANSYS	
1	224.1	227.0	1.3	227.1	230.0	1.3	230.1	233.0	1.3	233.0	236.0	1.3
2	224.0	227.0	1.3	227.0	230.0	1.3	229.9	233.0	1.3	232.8	236.0	1.4
3	227.0	227.0	0.0	230.0	230.0	0.0	233.0	233.0	0.0	236.0	236.0	0.0
4	225.4	227.0	0.7	228.4	230.0	0.7	231.4	233.0	0.7	234.4	236.0	0.7
5	224.5	227.0	1.1	227.5	230.0	1.1	230.5	233.0	1.1	233.5	236.0	1.1

A7. General transport equations:

Equation (A4) [14, 15] illustrates the species balance or continuity relation in Cartesian coordinates for the fibre.

$$\left(\frac{\partial C_{fg}}{\partial t} + v_x \frac{\partial C_{fg}}{\partial x} + v_y \frac{\partial C_{fg}}{\partial y} + v_z \frac{\partial C_{fg}}{\partial z}\right) = - \left[\frac{\partial J_{xfg}}{\partial x} + \frac{\partial J_{yfg}}{\partial y} + \frac{\partial J_{zfg}}{\partial z} \right] + r_{fg} \quad (\text{A4})$$

where fg is the identification number of each species (the functional group in this study), including $-\text{C}\equiv\text{N}$, $-\text{C}=\text{N}-$, $-\text{CH}_2$, $-\text{C}=\text{C}-$, and $-\text{C}=\text{O}$. The other functional groups have been considered as inert and are not taken into account. t , x , y , and z are time and space coordinates.

Moreover, J is mass flux ($\text{kg}/\text{s} \cdot \text{m}^2$) [14]:

$$J_{xfg} = -D_e \frac{\partial C_{fg}}{\partial x}, \quad J_{yfg} = -D_e \frac{\partial C_{fg}}{\partial y} \quad \text{and} \quad J_{zfg} = -D_e \frac{\partial C_{fg}}{\partial z} \quad (\text{A5})$$

A8. Reduction of C=O bands in preliminary steps:

Fig. A13 has been produced based on a complete deconvolution analysis on FT-IR ATR spectra of PAN precursor and OPF samples in the preliminary step of the thermal oxidative stabilisation process. For more information regarding the samples, procedures, and results, please refer to our previous publication [13].

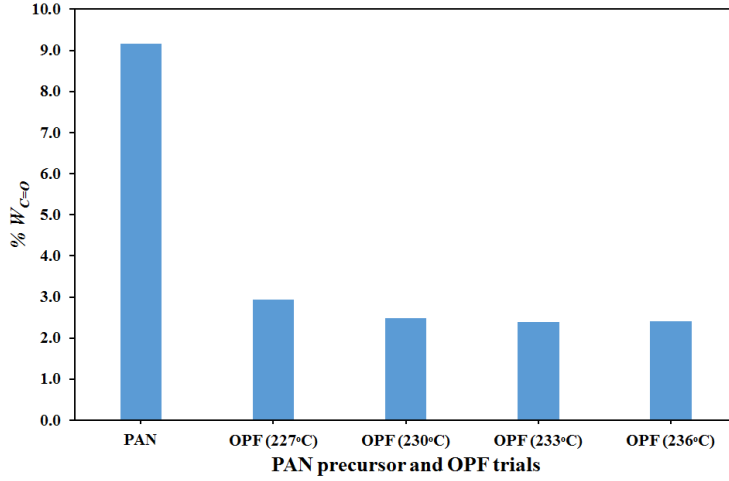


Fig. A13. Changes on the percentage of carbon – oxygen double bonds functional groups based on deconvoluted results of FT-IR ATR spectroscopy, during the preliminary steps of thermal oxidative stabilization process in various temperature, at space velocity 25 m/h and stretching ratio 3%.

A9. Discretised equations:

Equations 13 to 17e were discretised and summarized as below based on the 3D mesh grid structure of tow (Fig. 2b):

$$\frac{v_x}{2\Delta\xi.l.\rho_{O_2}} Y_{(-C\equiv N)}^{i+1,j,k} - \frac{v_x}{2\Delta\xi.l.\rho_{O_2}} Y_{(-C\equiv N)}^{i-1,j,k} + k_1^{i,j,k} \cdot Y_{(-C\equiv N)}^{i,j,k} \cdot Y_{O_2}^{i,j,k} = 0 \quad (A6)$$

$$\frac{v_x}{2\Delta\xi.l.\rho_{O_2}} Y_{(-CH_2)}^{i+1,j,k} - \frac{v_x}{2\Delta\xi.l.\rho_{O_2}} Y_{(-CH_2)}^{i-1,j,k} + (k_2^{i,j,k} + k_3^{i,j,k}) \cdot Y_{(-CH_2)}^{i,j,k} \cdot Y_{O_2}^{i,j,k} - k_4^{i,j,k} \cdot Y_{(-C=O)}^{i,j,k} \cdot Y_{O_2}^{i,j,k} = 0 \quad (A7)$$

$$\frac{v_x}{2\Delta\xi.l.\rho_{O_2}} Y_{(-C=N)}^{i+1,j,k} - \frac{v_x}{2\Delta\xi.l.\rho_{O_2}} Y_{(-C=N)}^{i-1,j,k} - k_1^{i,j,k} \cdot Y_{(-C\equiv N)}^{i,j,k} \cdot Y_{O_2}^{i,j,k} = 0 \quad (A8)$$

$$\frac{v_x}{2\Delta\xi.l.\rho_{O_2}} Y_{(C=C)}^{i+1,j,k} - \frac{v_x}{2\Delta\xi.l.\rho_{O_2}} Y_{(C=C)}^{i-1,j,k} - k_2^{i,j,k} \cdot Y_{(-CH_2)}^{i,j,k} \cdot Y_{O_2}^{i,j,k} = 0 \quad (A9)$$

$$\frac{v_x}{2\Delta\xi.l.\rho_{O_2}} Y_{(C=O)}^{i+1,j,k} - \frac{v_x}{2\Delta\xi.l.\rho_{O_2}} Y_{(C=O)}^{i-1,j,k} - k_3^{i,j,k} \cdot Y_{(-CH_2)}^{i,j,k} \cdot Y_{O_2}^{i,j,k} + k_4^{i,j,k} \cdot Y_{(-C=O)}^{i,j,k} \cdot Y_{O_2}^{i,j,k} = 0 \quad (A10)$$

$$\begin{aligned}
& \left(\frac{v_x}{2\Delta\xi.l.\rho_{PAN}} - \frac{De_{O_2}}{l^2(\Delta\xi)^2.\rho_{PAN}} \right) Y_{O_2}^{i+1,j,k} + \frac{De_{O_2}}{w^2(\Delta\zeta)^2.\rho_{PAN}} Y_{O_2}^{i,j+1,k} + \frac{De_{O_2}}{h^2(\Delta\eta)^2.\rho_{PAN}} Y_{O_2}^{i,j,k+1} + \\
& \left(\frac{2De_{O_2}}{l^2(\Delta\xi)^2.\rho_{PAN}} + \frac{2De_{O_2}}{w^2(\Delta\zeta)^2.\rho_{PAN}} + \frac{2De_{O_2}}{h^2(\Delta\eta)^2.\rho_{PAN}} + (k_2^{i,j,k} + k_3^{i,j,k}) \cdot Y_{(-CH_2)}^{i,j,k} - \right. \\
& \left. k_4^{i,j,k} \cdot Y_{(-C=O)}^{i,j,k} \right) Y_{O_2}^{i,j,k} - \left(\frac{v_x}{2\Delta\xi.l.\rho_{PAN}} + \frac{De_{O_2}}{l^2(\Delta\xi)^2.\rho_{PAN}} \right) Y_{O_2}^{i-1,j,k} - \frac{De_{O_2}}{w^2(\Delta\zeta)^2.\rho_{PAN}} Y_{O_2}^{i,j-1,k} - \\
& \frac{De_{O_2}}{h^2(\Delta\eta)^2.\rho_{PAN}} Y_{O_2}^{i,j,k-1} = 0
\end{aligned} \tag{A11}$$

for boundaries at $y = 0$,

$$3Y_{O_2}^{i,j,k} - 4Y_{O_2}^{i,j+1,k} + Y_{O_2}^{i,j+2,k} = 0 \tag{A12a}$$

$$3Y_{fg}^{i,j,k} - 4Y_{fg}^{i,j+1,k} + Y_{fg}^{i,j+2,k} = 0 \tag{A12b}$$

for boundaries at $z = 0$,

$$3Y_{O_2}^{i,j,k} - 4Y_{O_2}^{i,j,k+1} + Y_{O_2}^{i,j,k+1} = 0 \tag{A13a}$$

$$3Y_{fg}^{i,j,k} - 4Y_{fg}^{i,j,k+1} + Y_{fg}^{i,j,k+1} = 0 \tag{A13b}$$

for boundaries at $y = z = 0$,

$$6Y_{O_2}^{i,j,k} - 4Y_{O_2}^{i,j+1,k} - 4Y_{O_2}^{i,j,k+1} + Y_{O_2}^{i,j+2,k} + Y_{O_2}^{i,j,k+1} = 0 \tag{A14a}$$

$$6Y_{fg}^{i,j,k} - 4Y_{fg}^{i,j+1,k} - 4Y_{fg}^{i,j,k+1} + Y_{fg}^{i,j+2,k} + Y_{fg}^{i,j,k+1} = 0 \tag{A14b}$$

for boundaries at $x = l$,

$$\left(\frac{3v_x}{2\Delta\xi.l.\rho_{O_2}} + k_1^{i,j,k} \cdot Y_{O_2}^{i,j,k} \right) Y_{(-C\equiv N)}^{i,j,k} - \frac{2v_x}{\Delta\xi.l.\rho_{O_2}} Y_{(-C\equiv N)}^{i-1,j,k} + \frac{v_x}{2\Delta\xi.l.\rho_{O_2}} Y_{(-C\equiv N)}^{i-2,j,k} = 0 \tag{A15}$$

$$\left(\frac{3v_x}{2\Delta\xi.l.\rho_{O_2}} + (k_2^{i,j,k} + k_3^{i,j,k}) Y_{O_2}^{i,j,k} \right) Y_{(CH_2)}^{i,j,k} - \frac{2v_x}{\Delta\xi.l.\rho_{O_2}} Y_{(-CH_2)}^{i-1,j,k} + \frac{v_x}{2\Delta\xi.l.\rho_{O_2}} Y_{(-CH_2)}^{i-2,j,k} = 0 \tag{A16}$$

$$\frac{3v_x}{2\Delta\xi.l.\rho_{O_2}} Y_{(-C=N)}^{i,j,k} - \frac{2v_x}{\Delta\xi.l.\rho_{O_2}} Y_{(-C=N)}^{i-1,j,k} + \frac{v_x}{2\Delta\xi.l.\rho_{O_2}} Y_{(-C=N)}^{i-2,j,k} - k_1^{i,j,k} \cdot Y_{(-C\equiv N)}^{i,j,k} \cdot Y_{O_2}^{i,j,k} = 0 \tag{A17}$$

$$\frac{3v_x}{2\Delta\xi.l.\rho_{O_2}} Y_{(C=C)}^{i,j,k} - \frac{2v_x}{\Delta\xi.l.\rho_{O_2}} Y_{(C=C)}^{i-1,j,k} + \frac{v_x}{2\Delta\xi.l.\rho_{O_2}} Y_{(C=C)}^{i-2,j,k} - k_2^{i,j,k} \cdot Y_{(-CH_2)}^{i,j,k} \cdot Y_{O_2}^{i,j,k} = 0 \tag{A18}$$

$$\begin{aligned}
& \left(\frac{3v_x}{2\Delta\xi.l.\rho_{O_2}} + k_4^{i,j,k} \cdot Y_{O_2}^{i,j,k} \right) Y_{(C=O)}^{i,j,k} - \frac{v_x}{2\Delta\xi.l.\rho_{O_2}} Y_{(C=O)}^{i-1,j,k} + \frac{v_x}{2\Delta\xi.l.\rho_{O_2}} Y_{(C=O)}^{i-2,j,k} - \\
& k_3^{i,j,k} \cdot Y_{(-CH_2)}^{i,j,k} \cdot Y_{O_2}^{i,j,k} = 0
\end{aligned} \tag{A19}$$

$$\begin{aligned}
& \frac{D_{eO_2}}{w^2(\Delta\zeta)^2 \cdot \rho_{PAN}} Y_{O_2}^{i,j+1,k} + \frac{D_{eO_2}}{h^2(\Delta\eta)^2 \cdot \rho_{PAN}} Y_{O_2}^{i,j,k+1} + \left(\frac{3v_x}{2\Delta\xi \cdot l \cdot \rho_{PAN}} - \frac{2D_{eO_2}}{l^2(\Delta\xi)^2 \cdot \rho_{PAN}} + \frac{2D_{eO_2}}{w^2(\Delta\zeta)^2 \cdot \rho_{PAN}} + \right. \\
& \left. \frac{2D_{eO_2}}{h^2(\Delta\eta)^2 \cdot \rho_{PAN}} + (k_2^{i,j,k} + k_3^{i,j,k}) \cdot Y_{(-CH_2)}^{i,j,k} - k_4^{i,j,k} \cdot Y_{(-C=O)}^{i,j,k} \right) Y_{O_2}^{i,j,k} - \left(\frac{2v_x}{\Delta\xi \cdot l \cdot \rho_{PAN}} - \right. \\
& \left. \frac{5D_{eO_2}}{l^2(\Delta\xi)^2 \cdot \rho_{PAN}} \right) Y_{O_2}^{i-1,j,k} - \frac{D_{eO_2}}{l^2(\Delta\zeta)^2 \cdot \rho_{PAN}} Y_{O_2}^{i,j-1,k} - \frac{D_{eO_2}}{h^2(\Delta\eta)^2 \cdot \rho_{PAN}} Y_{O_2}^{i,j,k-1} + \left(\frac{v_x}{2\Delta\xi \cdot l \cdot \rho_{PAN}} - \right. \\
& \left. \frac{4D_{eO_2}}{l^2(\Delta\xi)^2 \cdot \rho_{PAN}} \right) Y_{O_2}^{i-2,j,k} + \frac{D_{eO_2}}{l^2(\Delta\xi)^2 \cdot \rho_{PAN}} Y_{O_2}^{i-3,j,k} = 0
\end{aligned} \tag{A20}$$

The oxygen concentration was assumed constant in Equations A6 to A10 and A15 to A18 due to high concentration, but it was the main variable in Equations A11, A15a, A13a, A14a, and A20.

A10. Prediction of reaction rate parameters by DSC:

Ramp DSC experiments were done for prediction of reaction rate parameters based on Kissinger approach [8, 9] and FWO approach [10] in order to guess kinetics parameters as input for the first step of modelling. Figures A4 shows the results of DSC test for PAN precursor in different ramps (3, 5, 7, 10 and 20 °C/min).

Two different peaks were distinguished in these figures. The height of these peaks and their location on the horizontal axis were extracted from Fig. A14. These data were employed to estimate the rate of different reaction series. The DSC results were analysed based on both Kissinger approach (Equations A1 and A2) in Fig. A15, and FWO approach (Equations A2 and A3) in Fig. A16 by the least square method.

The results of the curve fitting method (least square approach) were presented in Table 3. There were differences between outcomes of Kissinger and FWO approaches, regarding the assumption and approximations that were used for governing Equations A1 to A3. We employed the average of these data (Table 3) similar to other researchers [10, 16].

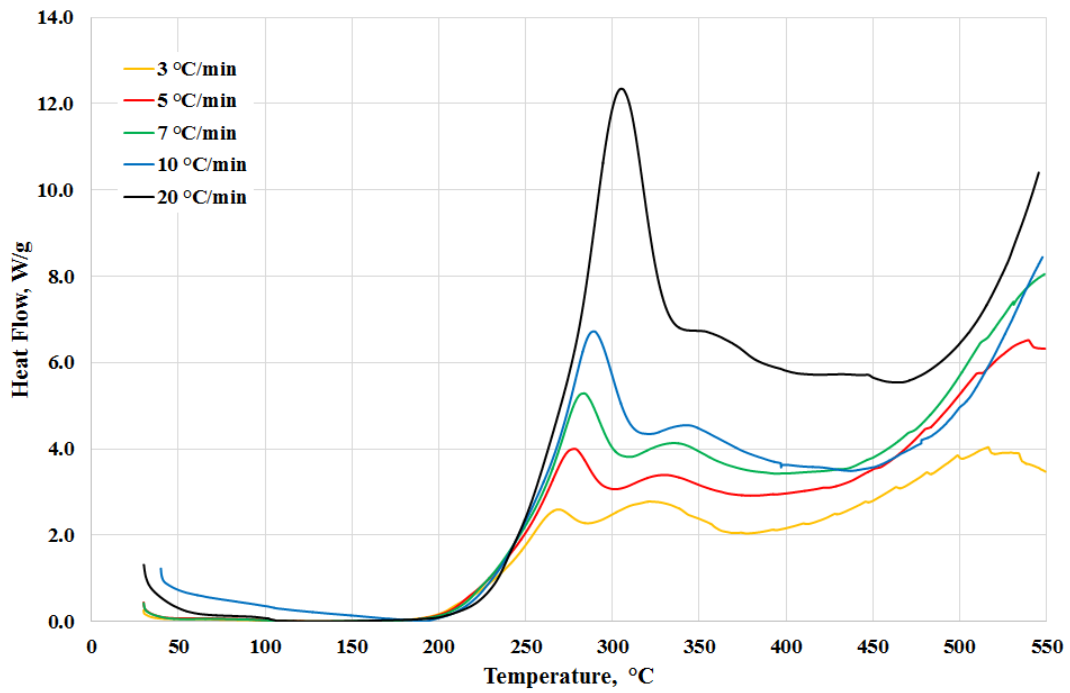


Fig. A14. DSC Results of PAN precursor based on various ramps, heat flow vs temperature.

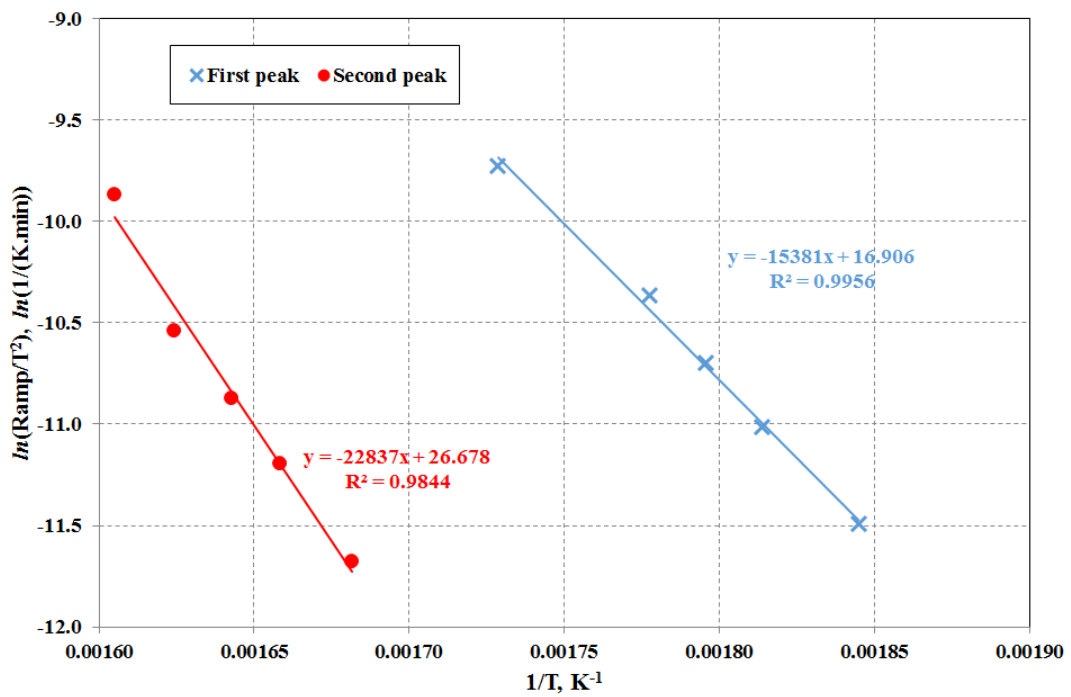


Fig. A15. Analysis of DSC results based on Kissinger approach.

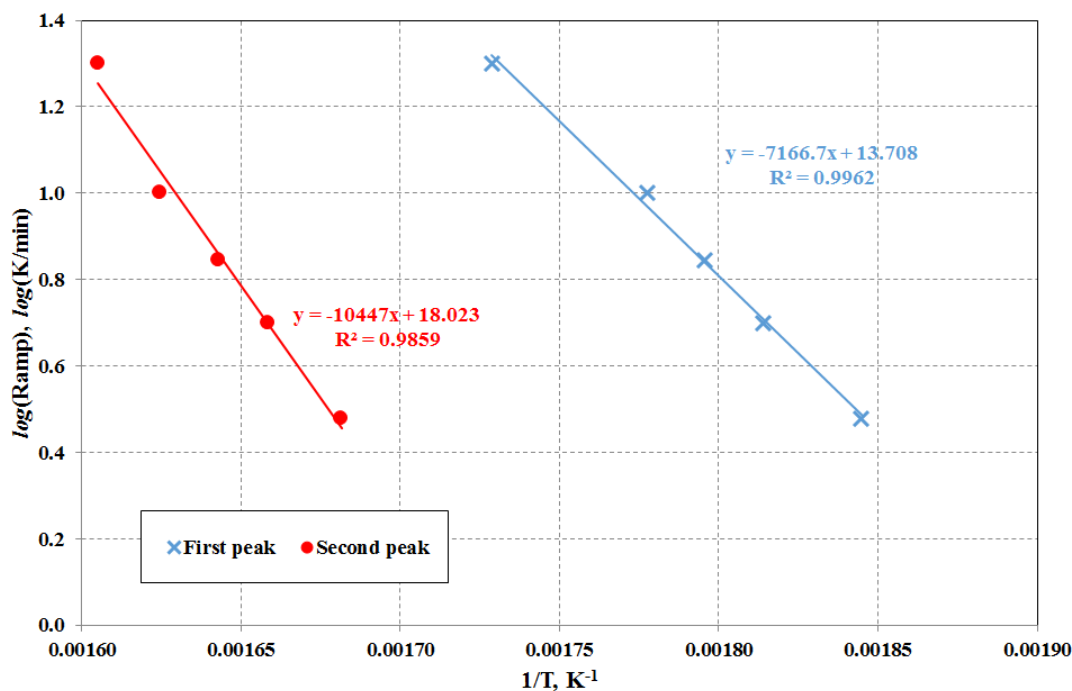


Fig. A16. Analysis of DSC results based on the FWO approach.

A11. The range of operating temperatures:

Because of the significance of temperature on kinetic parameters [17], the first step of this study is to find the effective range of temperature. DSC is a relevant laboratory equipment for this purpose. Therefore, around 2.5 mg of PAN precursor was weighted with 0.0001 mg accuracy and was isothermally tested in the atmospheric environment (presence of oxygen) under various temperature conditions.

Fig. A17 shows the results of these tests at isothermal conditions from 130°C (far from the normal boiling point of water) to 250°C. These results show no significant reaction lower than 200°C. In this temperature, a sudden increase was observed in the production of heat flow that gradually decreased as the tests continued. This changed to a peak shape with a maximum in a temperature range of more than 200°C. The peak became sharper with the increase in temperature. At around 250°C, it was very near to Dirac delta function and disclosed a very fast reaction similar to combustion. Thus, four different levels of temperature, 227, 230, 233,

and 236°C, were selected as the operating temperature based on the DSC results and the available experience.

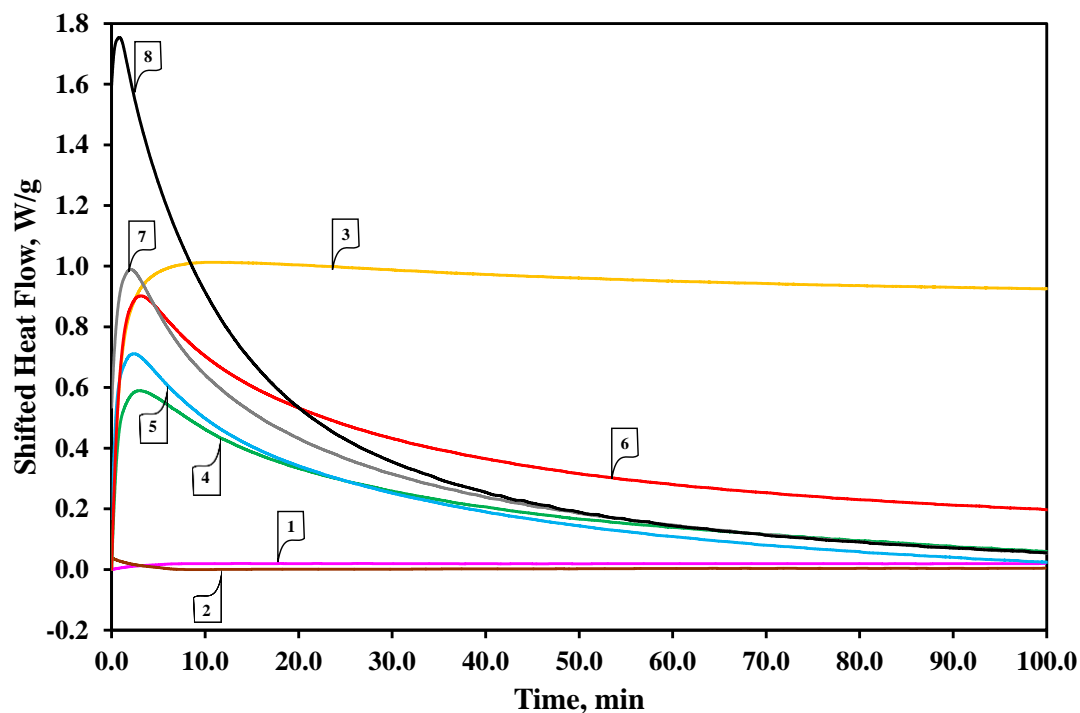


Fig. A17. Results of isothermal DSC experiments at (1) 130°C, (2) 150°C, (3) 200°C, (4) 227°C, (5) 230°C, (6) 233°C, (7) 236°C, and (8) 250°C.

References:

1. Z. Bashir, Carbon, 1991, 29, 1081.
2. M.S.A. Rahaman, A.F. Ismail, A. Mustafa, Polym. Degrad. Stab., 2007, 92, 1421.
3. E. Fitzer, D.J. Müller, Carbon, 1975, 13, 63.
4. S. Kim, Y.S. Chung, H.S. Choi, F.L. Jin, S.J. Park, Bull. Korean Chem. Soc., 2013, 34, 3733.
5. E. Fitzer, W. Frohs, M. Heine, Carbon, 1986, 24, 387.

6. H. Khayyam, M. Naebe, O. Zabihi, R. Zamani, S. Atkiss, B. Fox, *IEEE Trans. Indust. Inform.*, 2015, 11, 887.
7. E. Fitzer, *Carbon*, 1989, 27, 621.
8. H.E. Kissinger, *J. Res. Nation. Bur. Stand.*, 1956, 57, 217.
9. H.E. Kissinger, *Anal. Chem.*, 1957, 29, 1702.
10. L. Zhang, Y. Dai, Y. Kai, R.-G. Jin, *Carbon Lett.*, 2011, 12, 229.
11. J.H. Flynn, L.A. Wall, A quick, *J. Polym. Sci. B: Polym. Lett.*, 1966, 4, 323.
12. T. Ozawa, *Bull. Chem. Soc. Jap.*, 1965, 38, 1881.
13. K. Badii, J.S. Church, G. Golkarnarenji, M. Naebe, H. Khayyam, *Polym. Degrad. Stab.*, 2016, 131, 53.
14. R.B. Bird, W.E. Stewart, E.N. Lightfoot, *Transport Phenomena*, Wiley, USA, 2007.
15. M.G. Dunham, D.D. Edie, *Carbon*, 1992, 30, 435.
16. Y. Liu, H.G. Chae, S. Kumar, *Carbon*, 2011, 49, 4477.
17. O. Levenspiel, *Chemical reaction engineering*, 3rd ed., John Wiley & Sons, USA, 1999.